

# Fluid dynamics of planetary ices

RALF GREVE\*

Institute of Low Temperature Science, Hokkaido University,  
Kita-19, Nishi-8, Kita-ku, Sapporo 060-0819, Japan

## Abstract

The role of water ice in the solar system is reviewed from a fluid-dynamical point of view. On Earth and Mars, water ice forms ice sheets, ice caps and glaciers at the surface, which show glacial flow under their own weight. By contrast, water ice is a major constituent of the bulk volume of the icy satellites in the outer solar system, and ice flow can occur as thermal convection. The rheology of polycrystalline aggregates of ordinary, hexagonal ice Ih is described by a power law, different forms of which are discussed. The temperature dependence of the ice viscosity follows an Arrhenius law. Therefore, the flow of ice in a planetary environment constitutes a thermo-mechanically coupled problem; its model equations are obtained by inserting the flow law and the thermodynamic material equations in the balance laws of mass, momentum and energy. As an example of gravity-driven flow, the polar caps of Mars are discussed. For the north-polar cap, large-scale flow velocities of the order of  $0.1 \dots 1 \text{ mm a}^{-1}$  are likely, locally enhanced by a factor ten or more in the vicinity of surface scarps/troughs. By contrast, the colder south-polar cap is expected to be almost stagnant. Tidally heated convection is discussed for the example of the icy crust of Europa, where a two-dimensional model predicts the formation of an upper, conductive lid and a lower, convective layer with flow velocities of the order of  $100 \text{ mm a}^{-1}$ . Very little is known about the fluid-dynamical relevance of high-pressure phases of water ice as well as ices made up of other materials.

## 1 Introduction

Water ice is an abundant material in the solar system. In the inner solar system, it plays an important role on Earth and on Mars, where it forms a cryosphere as an active, dynamic part of the respective climate system. Approximately 10% of the land surface of the present-day Earth, or  $14.6 \times 10^6 \text{ km}^2$ , are covered by ice sheets, ice caps and glaciers, the total volume of which is approximately  $28.7 \times 10^6 \text{ km}^3$  [4]. By far the largest single ice body is the Antarctic ice sheet, which alone contains about 90% of this ice. All of these terrestrial ice bodies are subject to gravity-driven glacial flow with typical velocities of tens to hundreds of meters per year. Further components of the terrestrial cryosphere are the floating ice shelves and sea ice, seasonal snow and ground ice (permafrost).

---

\*E-mail: greve@lowtem.hokudai.ac.jp

The ice sheets, ice shelves, ice caps and glaciers have formed by accumulated snowfall over centuries, millenia and more. Over these time-scales, the Earth's climate has experienced significant changes known as glacial-interglacial cycles, which are driven by periodic changes of the orbital parameters obliquity (axial tilt), eccentricity and precession ("Milankovitch cycles"). The last 800,000 years have been characterized by a strong dominance of the 100,000-year eccentricity cycle [29], with a sequence of shorter interglacials (warm periods) like the current Holocene and longer glacials (ice ages). At the last glacial maximum approximately 20,000 years ago, large parts of north America and Eurasia were covered by ice sheets which no longer exist, and the global ice volume was about three times larger than at present.

On Mars, the polar ice caps are one of the most prominent surface features. The seasonal caps, which can extend down to latitudes of approximately  $55^{\circ}\text{N/S}$ , consist of only some ten centimeters of  $\text{CO}_2$  snow which sublimates into the atmosphere during the respective spring season. By contrast, the smaller residual caps poleward of approximately  $80^{\circ}\text{N/S}$  survive the summer seasons, and they are underlain by massive topographic structures, which are known as the polar layered deposits [34]. The residual caps and the underlying layered deposits are considered to be geomorphological units and shall be referred to as the north- and south-polar cap (NPC/SPC), respectively. The Mars Orbiter Laser Altimeter (MOLA) measurements of the Mars Global Surveyor (MGS) spacecraft have provided a very precise mapping of the surface topographies of the polar caps [32, 40]. Combined with the estimated cap margins and equilibrated ground topographies discussed later (Sect. 4.1), this yields for the NPC a volume of about  $1.2 \times 10^6 \text{ km}^3$  and an area of  $1.1 \times 10^6 \text{ km}^2$ , and for the SPC a volume of  $1.8 \times 10^6 \text{ km}^3$  and an area of  $1.7 \times 10^6 \text{ km}^2$ . Due to isostatic deflection of the underlying lithosphere, the real volumes may be up to 30% larger. In any case, the NPC and SPC are the largest known water reservoirs on Mars. Further constituents may be dust,  $\text{CO}_2$  ice and  $\text{CO}_2$  clathrate hydrate. Comparable or even larger amounts of water may be stored as permafrost in the ground [5]; an idea which was corroborated by the spectrometric detection of mid- and high-latitude subsurface layers enriched in hydrogen, interpreted as ground ice [2].

Similar to the situation on Earth, the Martian polar caps are active components of the climate system which interact with the atmosphere thermally, orographically and by condensation and sublimation processes of water vapour. Their present topographies are the result of the climatic history over at least the last millions of years, which were probably characterized by climate cycles as a consequence of strong, quasi-periodic variations of the orbital parameters obliquity, eccentricity and precession on time-scales of  $10^5$ – $10^6$  years [19]. This idea is supported by the light-dark layered deposits of the polar caps, which are exposed in the scarps and troughs in the ice surface and close to the margins, and which indicate a strongly varying dust content of the ice due to varying atmospheric conditions in the past. Further, Head et al. [15] suggested that Mars underwent "ice ages" during periods of high obliquity like that from about 2.1 to 0.4 million years ago (with obliquity maxima of  $\approx 35^{\circ}$ ). These ice ages are supposedly characterized by warmer polar climates, enhanced mass loss of the polar caps due to sublimation and the formation of meters-thick ice deposits equatorward to approximately  $30^{\circ}\text{N/S}$ .

For the Moon and Mercury, which are both devoid of any significant atmosphere and therefore subject to intensive solar radiation, water ice may be cold-trapped inside permanently shadowed craters at the poles, which is possible due to the very small tilts of

the rotational axes. Some evidence for this idea was provided by the space-probe Lunar Prospector, which detected hydrogen in the vicinity of the lunar poles by neutron spectrometry [7], and, for the case of Mercury, by terrestrial radar mapping which revealed a highly reflective region on the north pole [31].

In the outer solar system (beyond the asteroid belt), owing to the very low temperatures, evaporation of water ice at the surface of planetary bodies becomes so small that this substance survives for time-spans comparable to the age of the solar system [39]. Therefore, while in the inner solar system the geological evolution of the planets is dominated by rock material, the history of a large number of bodies in the outer solar system is dominated by water ice and other moderately volatile substances. Of course, this statement does not hold for the giant planets, which do not have a solid surface and are made up of highly volatile substances, mainly hydrogen and helium. Thus, it refers to the large moons of the Jovian, Saturnian, Uranian and Neptunian systems, Pluto and smaller moons, asteroids and planetary ring particles. Of particular interest are the Jovian moon Europa, for which there is strong evidence for an outer icy shell underlain by a deep ocean [18], and the Saturnian moon Titan, for which the findings of the recently landed space-probe Huygens suggest a solid surface made up mainly of water ice and a methane hydrosphere with rainfall, rivers and seas (see <http://huygens.esa.int>).

In this review paper, the focus will be on *flowing* water ice, which can be driven either by gravity forces or by thermal convection. The layout is as follows. In Sect. 2, the rheology of polycrystalline aggregates of water ice is discussed, including the effects of different creep mechanisms, partial melting and impurities (dust), and suitable flow laws (stress-strain-rate relations) are given. This allows the formulation of a closed set of model equations for the thermo-mechanically coupled problem of ice flow, which is done in Sect. 3. Applications to the Martian polar caps are presented in Sect. 4. New results are shown for their large-scale dynamics under assumed steady-state conditions (Sect. 4.1), and the local influence of the prominent scarps and troughs in the surface is treated (Sect. 4.2). Simulations on tidally heated convection in the icy shell of Europa are discussed in Sect. 5. Finally, Sect. 6 concludes the paper.

## 2 Ice rheology

### 2.1 Structure of ice

Water ice can exist in a great variety of different phases (Fig. 1, Ref. [26]). Most of these phases form under high pressure, which results in a denser packing of the water molecules compared to the “ordinary” ice Ih. The stability range of the latter is for pressures  $P \lesssim 200$  MPa, which is equivalent to the hydrostatic pressure of an ice layer (density  $\rho_i = 910 \text{ kg m}^{-3}$ ) of approximately 22 km on Earth (gravity acceleration  $g = 9.81 \text{ m s}^{-2}$ ), 60 km on Mars ( $g = 3.72 \text{ m s}^{-2}$ ) and 165 km on Europa ( $g = 1.32 \text{ m s}^{-2}$ ) and Titan ( $g = 1.35 \text{ m s}^{-2}$ ). We will limit our discussions to the outer shells of the planetary bodies, so that only ice Ih needs to be considered in the following.

Ice Ih forms hexagonal crystals, that is, the water molecules are arranged in layers of hexagonal rings (Fig. 2, Ref. [25]). The plane of such a layer is called the basal plane, which actually consists of two planes shifted slightly (by 0.0923 nm) against each other.

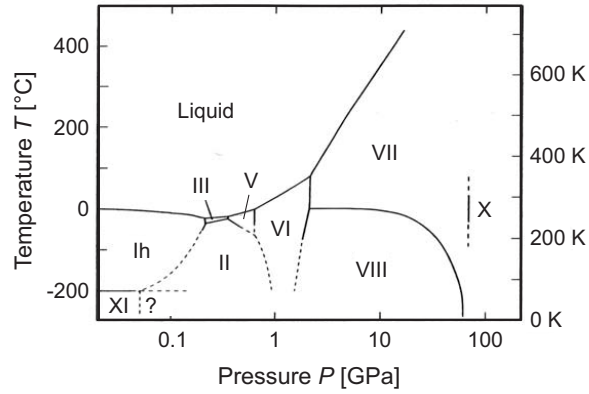


Figure 1: Phase diagram of the ice-water system. Only stable phases are shown. Figure by Petrenko and Whitworth [26, their Fig. 11.2 on p. 253].

The direction perpendicular to the basal planes is the optic axis or  $c$ -axis, and the distance between two subsequent basal planes is 0.276 nm. This leads to the very low packing factor of 34%, which is responsible for the density anomaly of ice Ih (smaller density than liquid water). Further, the basal planes can glide on each other when a shear stress is applied, comparable to the deformation of a deck of cards. This effect is strongly enhanced by the existence and generation of dislocations (structural defects) in real crystals, and the mechanism is consequently called *dislocation creep*.

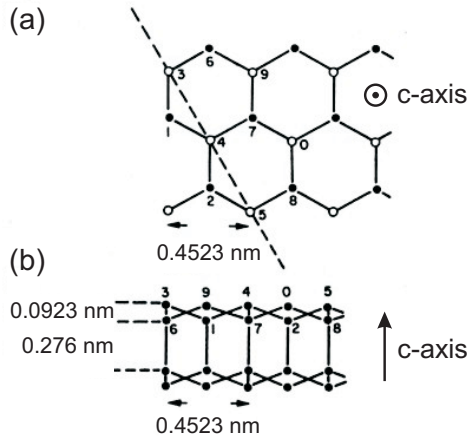


Figure 2: Structure of an ice crystal. The circles denote the oxygen atoms of the  $H_2O$  molecules. (a) Projection on the basal plane. (b) Projection on plane indicated by the broken line in (a). Figure by Paterson [25, his Fig. 5.1 on p. 80].

On the macro-scale, ice aggregates on planetary bodies (grounded ice sheet/cap/glacier, ground ice, floating ice shell etc.) are composed of a vast number of individual crystals. For instance, for terrestrial ice sheets and glaciers, the typical grain size is of the order of millimeters to centimeters. Such a compound is called *polycrystalline ice*. At the time of formation, it can be assumed that the orientation of the crystals is completely at random, so that the macroscopic behaviour of the compound will be isotropic. Ice-core studies on

Earth have revealed that in the course of time anisotropic fabrics can develop due to the strain history which a piece of ice experiences during its motion in an ice sheet or glacier (e.g. [1, 35]; see also [28, this volume]). However, since essentially nothing is known about the fabric of extraterrestrial ice bodies, we will assume isotropic conditions for simplicity in the following.

## 2.2 Pressure melting point

The melting temperature of pure ice Ih depends on the pressure  $P$ . It can therefore be written as

$$T_m = T_0 - f(P), \quad (1)$$

where  $T_0 = 273.16$  K is the melting temperature for  $P_0 = 611.657$  Pa, that is, at the triple point of water. According to [38], the melting-point depression  $f(P)$  is in implicit form

$$\frac{P}{P_0} = 1 - 626,000 (1 - \Theta^{-3}) + 197,135 (1 - \Theta^{21.2}), \quad (2)$$

$$\Theta = \frac{T_m}{T_0} = \frac{T_0 - f(P)}{T_0},$$

where  $P_0 \leq P \leq 209.9$  MPa and  $T_0 \geq T_m \geq 251.165$  K (Fig. 3). For moderate pressures, Eq. (2) can be linearized as

$$f(P) = \beta P, \quad (3)$$

where  $\beta = 7.42 \times 10^{-8}$  K Pa $^{-1}$  is the Clausius-Clapeyron constant for pure ice [25]. The error of this linearization is negligible for  $P \leq 10$  MPa, less than 10% for  $P \leq 50$  MPa and approximately 30% for  $P \approx 200$  MPa (Fig. 3).

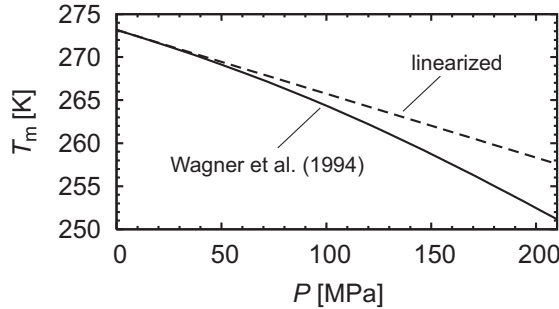


Figure 3: Pressure melting point of ice Ih by Wagner et al. [38] [Eq. (2), solid line] and linearized relation (3) (dashed line).

Impurities of different kinds alter the melting point further. For terrestrial, air-saturated glacier ice, Paterson [25] reports a modified Clausius-Clapeyron constant of  $\beta = 9.8 \times 10^{-8}$  K Pa $^{-1}$  for the linearized melting-point depression (3). If salts are present, an additional melting-point depression occurs which depends on the type of salts and their concentration. Intermixtures of ammonia, which may play a role in a supposed subsurface ocean on Titan below an outer ice-Ih layer [33, and references therein], have a similar effect.

## 2.3 Flow of polycrystalline ice

When a specimen of polycrystalline ice is subjected to a constant normal or shear stress, it responds with a permanent deformation, which continues as long as the stress is applied. Typically, an initial, instantaneous elastic deformation of the polycrystalline aggregate is followed by a phase called primary creep during which the strain rate decreases continuously. This behaviour is related to the increasing geometric incompatibilities of the deforming single crystals with different orientations. After some time, a minimum strain rate is reached which remains constant in the following, so that the strain increases linearly with time. This phase is known as secondary creep. Especially in case of high temperatures ( $\gtrsim -10^\circ\text{C}$ ), at a later stage dynamic recrystallisation (nucleation and growth of crystals which are favourably oriented for deformation) sets in, which leads to accelerated creep and finally a constant strain rate significantly larger than that of the secondary creep. This is called tertiary creep (Fig. 4, Ref. [25]). Therefore, it can be assumed in good approximation that in deforming ice masses secondary creep prevails for low temperatures ( $\lesssim -10^\circ\text{C}$ ), whereas tertiary creep prevails for high temperatures ( $\gtrsim -10^\circ\text{C}$ ), so that the strain rate can be expressed as a unique function of the stress, the ice temperature and the pressure.

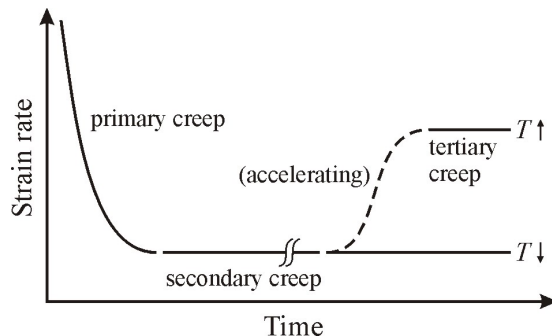


Figure 4: Creep response of a sample of polycrystalline ice to a constant stress for high ( $\gtrsim -10^\circ\text{C}$ , marked by  $T \uparrow$ ) and low ( $\lesssim -10^\circ\text{C}$ , marked by  $T \downarrow$ ) temperatures.

On the basis of these considerations, several forms of a non-linear viscous rheology for the flow of polycrystalline ice for different stress, strain-rate and temperature regimes have been proposed. They have in common to relate the strain-rate tensor  $\mathbf{D} = \text{sym grad } \mathbf{v}$  (velocity  $\mathbf{v}$ ) to the Cauchy stress deviator  $\mathbf{t}^D$ , and can be subsumed as

$$\mathbf{D} = EA(T, P) \frac{\sigma^{n-1}}{d^p} \mathbf{t}^D, \quad (4)$$

where  $\sigma = [\text{tr}(\mathbf{t}^D)^2/2]^{1/2}$  is the effective stress,  $n$  is the stress exponent,  $d$  is the grain size and  $p$  is the grain-size exponent (e.g. [6, 10, 12, 25, 37]). The flow rate factor  $A(T, P)$  depends via the Arrhenius law

$$A(T, P) = A_0 e^{-(Q+PV)/RT} \quad (5)$$

on the absolute temperature  $T$  and the pressure  $P$ , where  $A_0$  is the pre-exponential constant,  $Q$  is the activation energy,  $V$  is the activation volume and  $R = 8.314 \text{ J mol}^{-1} \text{ K}^{-1}$  is

the universal gas constant. The flow enhancement factor  $E$  is equal to unity for pure ice and can deviate from unity due to the softening or hardening effect of impurities in the ice. Since polycrystalline ice is described as a density-preserving (incompressible) medium, the pressure is a free field (not governed by a material equation), and the full Cauchy stress tensor  $\mathbf{t}$  is related to the traceless deviator  $\mathbf{t}^D$  by

$$\mathbf{t} = -P \mathbf{1} + \mathbf{t}^D, \quad (6)$$

where  $\mathbf{1}$  denotes the unity tensor.

Since appropriate values for the activation volume  $V$  are poorly constrained and the pressure effect is very small for typical thicknesses of ice sheets and caps, we account for it in an approximate way by setting  $V = 0$  and measuring the temperature relative to the pressure melting point  $T_m$  (see Sect. 2.2) instead. To this end, the *homologous temperature*

$$T' = T - T_m + T_0 = T + f(P) \quad (7)$$

is introduced, and the rate factor can be simplified as

$$A(T') = A_0 e^{-Q/RT'}, \quad (8)$$

which depends now exclusively on  $T'$  [25, 37]. For more details on this approach see Appendix A.

The general power law (4) can be inverted as follows. For the effective strain rate  $\delta = (\text{tr } \mathbf{D}^2/2)^{1/2}$  we obtain

$$\delta = EA(T') \frac{\sigma^n}{d^p}, \quad (9)$$

or equivalently, solved for  $\sigma$ ,

$$\sigma = [EA(T')]^{-1/n} d^{p/n} \delta^{1/n}. \quad (10)$$

Inserting this in (4) and solving for  $\mathbf{t}^D$  yields

$$\begin{aligned} \mathbf{t}^D &= [EA(T')]^{-1} d^p \left( [EA(T')]^{-1/n} d^{p/n} \delta^{1/n} \right)^{1-n} \mathbf{D} \\ &= [EA(T')]^{-1/n} \frac{d^{p/n}}{\delta^{1-1/n}} \mathbf{D}. \end{aligned} \quad (11)$$

By introducing the stress enhancement factor  $E_s = E^{-1/n}$  and the associated rate factor  $B(T') = [A(T')]^{-1/n}$ , this can be written as

$$\mathbf{t}^D = E_s B(T') \frac{d^{p/n}}{\delta^{1-1/n}} \mathbf{D}. \quad (12)$$

For terrestrial ice, the well-established Glen's flow law [which actually goes back to [23] in the general tensorial form] uses the stress exponent  $n = 3$ , the grain-size exponent  $p = 0$  and for the temperature range  $T' \leq 263$  K the pre-exponential constant  $A_0 = 3.985 \times 10^{-13} \text{ s}^{-1} \text{ Pa}^{-3}$  and the activation energy  $Q = 60 \text{ kJ mol}^{-1}$  [25]. The rheology defined by these parameters describes the grain-size-independent flow mechanism of dislocation creep, which prevails in terrestrial glaciers and ice sheets. The flow enhancement factor for ice

formed during glacial periods is often set to  $E = 3$ , interpreted as the softening influence of very small amounts of fine dust, approximately  $1 \text{ mg kg}^{-1}$  with particle sizes of  $0.1$  to  $2 \mu\text{m}$  [14]. This softening is attributed to thin films of liquid water which form around the dust particles and lubricate ice deformation. However, at the low temperatures expected in the NPC this effect will not be present, and direct hardening will be the dominant influence of dust (see Sect. 2.5).

Durham et al. [6] propose an alternative flow law for grain-size-independent dislocation creep, based on laboratory creep tests at a confining pressure of  $50 \text{ MPa}$ . For the temperature regime  $T = 195\text{--}240 \text{ K}$ , which corresponds approximately to  $T' = 200\text{--}245 \text{ K}$ , they report the parameters  $n = 4$ ,  $p = 0$ ,  $A_0 = 1.259 \times 10^{-19} \text{ s}^{-1} \text{ Pa}^{-4}$  and  $Q = 61 \text{ kJ mol}^{-1}$ .

However, for very low temperature and strain-rate conditions, as they are expected in the polar ice caps of Mars, it is not clear whether dislocation creep is still the predominant creep mechanism in the polycrystalline ice aggregate. There is evidence that other, grain-size-dependent flow mechanisms like grain-boundary sliding become favoured instead [10]. These can be described by the parameters  $n = 1.8$ ,  $p = 1.4$ ,  $A_0 = 6.20 \times 10^{-14} \text{ s}^{-1} \text{ Pa}^{-1.8} \text{ m}^{1.4}$  and  $Q = 49 \text{ kJ mol}^{-1}$  (see also [24]).

The relative contributions of the several flow laws (Glen, Durham, Goldsby-Kohlstedt; the latter will be abbreviated as ‘‘GK’’ in the following) can be estimated as follows. For simple shear in the  $x$ - $z$  plane and  $E = 1$ , Eq. (4) reduces to

$$\dot{\gamma} = 2A(T') \frac{\tau^n}{d^p}, \quad (13)$$

where  $\tau = t_{xz}^D$  is the shear stress and  $\dot{\gamma} = \partial v_x / \partial z = 2D_{xz}$  is the shear rate. Figure 5 shows the shear rates resulting from Eq. (13) for  $T' = 200 \text{ K}$  and the stress range from  $10 \text{ kPa}$  to  $100 \text{ MPa}$ . For GK, the grain sizes  $d = 1 \text{ mm}$  and  $10 \text{ mm}$  have been assumed, based on an estimate for the Martian north polar cap by Greve and Mahajan [12]. This range is also typical for terrestrial ice sheets and glaciers.

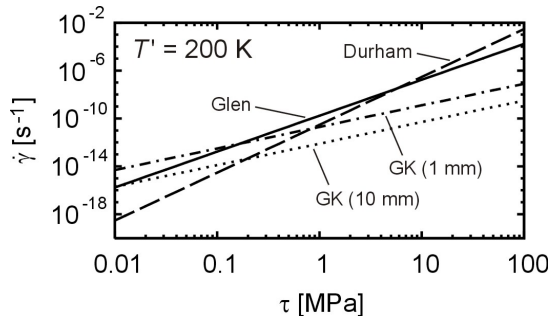


Figure 5: Shear rate  $\dot{\gamma}$  vs. shear stress  $\tau$  for simple shear, computed by Eq. (13) for  $T' = 200 \text{ K}$ . Flow laws: Glen ( $n = 3$ ), Durham ( $n = 4$ ), GK ( $n = 1.8$ ,  $p = 1.4$ ,  $d = 1 \text{ mm}$ ), GK ( $n = 1.8$ ,  $p = 1.4$ ,  $d = 10 \text{ mm}$ ).

It becomes evident that the relative contributions of the different flow laws vary strongly over this stress range. For low stresses, grain-size dependent flow with a low stress exponent (GK) dominates, whereas for higher stresses dislocation creep with a higher stress exponent (Glen, Durham) becomes more important. For the shown example with  $T' = 200 \text{ K}$ ,



the crossover stresses are 166.3 kPa for Glen/GK<sub>d=1 mm</sub>, 11.3 kPa for Glen/GK<sub>d=10 mm</sub>, 834.0 kPa for Durham/GK<sub>d=1 mm</sub> and 192.7 kPa for Durham/GK<sub>d=10 mm</sub>.

In order to account for the contributions of grain-size-independent dislocation creep and other, grain-size-dependent flow mechanisms simultaneously, a modified version of the flow law proposed by Pettit and Waddington [27] may be used. It sums up the two contributions via

$$\mathbf{D} = \left( E_1 A_1(T') \frac{\sigma^{n_1-1}}{d^{p_1}} + E_2 A_2(T') \frac{\sigma^{n_2-1}}{d^{p_2}} \right) \mathbf{t}^D, \quad (14)$$

where

$$A_1(T') = (A_0)_1 e^{-Q_1/RT'}, \quad A_2(T') = (A_0)_2 e^{-Q_2/RT'}. \quad (15)$$

In this representation, the index “1” refers to the parameters of either Glen’s or Durham’s flow law, the index “2” to those of the Goldsby-Kohlstedt flow law. However, this approach will not be further pursued here.

Note that, by introducing the *viscosity*  $\eta$ , the flow law (4) with the Arrhenius law in the form (8) can be written in compact form as

$$\mathbf{D} = \frac{1}{2\eta(T', \sigma, d)} \mathbf{t}^D, \quad \text{where } \eta(T', \sigma, d) = \frac{1}{2EA(T')} \frac{d^p}{\sigma^{n-1}}. \quad (16)$$

Similarly, the inverse flow law (12) reads

$$\mathbf{t}^D = 2\eta(T', \delta, d) \mathbf{D}, \quad \text{where } \eta(T', \delta, d) = \frac{E_s B(T')}{2} \frac{d^{p/n}}{\delta^{1-1/n}}. \quad (17)$$

Of course, the two representations of the viscosity in (16) and (17) are equivalent.

Evidently, for stress exponents  $n > 1$ , the viscosities (16), (17) become infinite in the low-stress/deformation limit  $\sigma, \delta \rightarrow 0$ , and there has been a long-standing debate whether this is physically acceptable. Also, some experimental evidence seems to indicate a Newtonian ( $n = 1$ ) rheology for this regime, even though these findings have been questioned (see the discussion by [25]). There are different possibilities of introducing a finite residual viscosity  $\eta_{\text{res}}$ . The effective stress  $\sigma$  and the effective strain rate  $\delta$  in the expressions (16), (17) can be replaced by  $\max(\sigma, \sigma_{\text{res}})$  and  $\max(\delta, \delta_{\text{res}})$ , respectively, where  $\sigma_{\text{res}}$  and  $\delta_{\text{res}}$  are small positive parameters. Alternatively, a small residual viscosity may be directly added,

$$\eta(T', \sigma, d) = \frac{1}{2EA(T')} \frac{d^p}{\sigma^{n-1}} + \eta_{\text{res}}, \quad (18)$$

or

$$\eta(T', \delta, d) = \frac{E_s B(T')}{2} \frac{d^{p/n}}{\delta^{1-1/n}} + \eta_{\text{res}}. \quad (19)$$

The disadvantage of these forms is that they are not equivalent anymore, and an inversion according to Eqs. (9)-(12) can no longer be executed.

## 2.4 Influence of liquid water

If the temperature of ice reaches the pressure melting point, liquid water may be present within the ice matrix, which is stored as lenses at the grain boundaries and in capillary

channels at triple grain junctions. Let  $\varphi_w$  be the volume fraction of water, then the density of the ice-water mixture is

$$\rho = (1 - \varphi_w)\rho_i + \varphi_w\rho_w, \quad (20)$$

where  $\rho_i = 910 \text{ kg m}^{-3}$  is the density of pure ice and  $\rho_w = 1000 \text{ kg m}^{-3}$  the density of pure water. Further, it is clear that the presence of liquid water will reduce the viscosity. Tobie et al. [36] propose an exponential softening, which can be expressed by a stress enhancement factor  $E_s < 1$ ,

$$E_s = e^{-b_w\varphi_w}, \quad (21)$$

or, equivalently, by a flow enhancement factor  $E > 1$ ,

$$E = E_s^{-n} = e^{nb_w\varphi_w}, \quad (22)$$

where  $b_w = 45$ . This value was chosen such that 5% melt decreases the viscosity in Eq. (17) by an order of magnitude, that is,  $E_s(\varphi_w = 0.05) = 0.1$ . In terrestrial glaciology, a linear relation reported by Paterson [25] has been widely used instead, which reads in terms of the enhancement factors

$$E = 1 + b_w\varphi_w \Leftrightarrow E_s = E^{-1/n} = (1 + b_w\varphi_w)^{-1/n}, \quad (23)$$

where  $b_w = \frac{580}{3.2} = 181.25$ . This relation has been established based on laboratory measurements for small water contents below 1% ( $\varphi_w < 0.01$ ).

## 2.5 Influence of dust

Satellite imagery shows that parts of the Martian polar ice caps appear dark, which indicates that they consist of ice with some amount of mixed-in dust. Greve and Mahajan [12] have laid down that this affects the ice flow in a multiple way, in that direct hardening can be partly compensated or even overcompensated by the increasing density, which increases the driving stresses, and the decreasing heat conductivity, which makes the ice at depth warmer and therefore softer. Therefore, the average volume fraction  $\varphi_d$  of dust is introduced, and the density,  $\rho$ , heat conductivity,  $\kappa$ , and specific heat,  $c$ , of the ice-dust mixture are computed as volume-fraction-weighted averages of the values for pure ice and crustal material,

$$\begin{aligned} \rho &= (1 - \varphi_d)\rho_i + \varphi_d\rho_c, \\ \kappa &= (1 - \varphi_d)\kappa_i + \varphi_d\kappa_c, \\ \rho c &= (1 - \varphi_d)\rho_i c_i + \varphi_d\rho_c c_c, \end{aligned} \quad (24)$$

with the following parameters: ice density  $\rho_i = 910 \text{ kg m}^{-3}$ , heat conductivity of ice  $\kappa_i = 9.828 e^{-0.0057 T[\text{K}]} \text{ W m}^{-1} \text{ K}^{-1}$ , specific heat of ice  $c_i = (146.3 + 7.253 T[\text{K}]) \text{ J kg}^{-1} \text{ K}^{-1}$ , density of crustal material (dust)  $\rho_c = 2900 \text{ kg m}^{-3}$ , heat conductivity of crustal material (dust)  $\kappa_c = 2.5 \text{ W m}^{-1} \text{ K}^{-1}$ , specific heat of crustal material (dust)  $c_c = 1000 \text{ J kg}^{-1} \text{ K}^{-1}$ . The additional density factors in Eq. (24)<sub>3</sub> are necessary because the averaging procedure requires volumetric quantities, whereas the specific heat is taken per mass unit.

Direct hardening is described by a stress enhancement factor  $E_s > 1$  based on laboratory measurements of the deformation of ice-dust compounds,

$$E_s = e^{b_d\varphi_d}, \quad (25)$$

where  $b_d = 2$  and  $\varphi_d \leq 0.56$  [6]. This is equivalent to a flow enhancement factor

$$E = E_s^{-n} = e^{-nb_d\varphi_d}. \quad (26)$$

Hence, for given stress, temperature and grain-size conditions and a stress exponent  $n = 3$  a dust content of 10% ( $\varphi_d = 0.1$ ) leads to an almost twice as hard material ( $E = 0.55$ ) compared to pure ice.

### 3 Model equations for ice flow

The thermo-mechanical problem of ice flow in a planetary environment can be described by the balance equations of mass, momentum and energy (e.g. [16]). For a density-preserving (incompressible) medium, which holds for ice in good approximation despite the variability expressed by Eqs. (20) and (24)<sub>1</sub>, the mass balance (continuity equation) reads

$$\operatorname{div} \mathbf{v} = 0. \quad (27)$$

For evolving ice bodies, it is convenient to vertically integrate the continuity equation. This yields the ice-thickness ( $H$ ) equation

$$\frac{\partial H}{\partial t} = -\operatorname{div} \mathbf{Q} + a_s - a_b, \quad (28)$$

where  $\mathbf{Q}$  is the volume flux (vertically integrated horizontal velocity), and  $a_s$  and  $a_b$  are the mass balances at the surface (positive for supply) and the bottom (positive for loss), respectively. The momentum balance yields with the flow law (17) the Stokes equation

$$-\operatorname{grad} P + \operatorname{div} [\eta (\operatorname{grad} \mathbf{v} + (\operatorname{grad} \mathbf{v})^T)] + \rho \mathbf{g} = \mathbf{0} \quad (29)$$

( $\mathbf{g}$ : vectorial gravity acceleration), in which the acceleration term  $\rho d\mathbf{v}/dt$  has been neglected due to the very low flow velocities to be expected. From the energy balance, Fourier's law of heat conduction

$$\mathbf{q} = -\kappa(T) \operatorname{grad} T \quad (30)$$

( $\mathbf{q}$ : heat flux,  $\kappa$ : heat conductivity) and the caloric equation of state

$$u = \int_{T_0}^T c(\bar{T}) d\bar{T} \quad (31)$$

( $u$ : specific internal energy,  $c$ : specific heat), the temperature-evolution equation

$$\rho c \left( \frac{\partial T}{\partial t} + \mathbf{v} \cdot \operatorname{grad} T \right) = \operatorname{div} (\kappa \operatorname{grad} T) + 4\eta \delta^2 + r \quad (32)$$

results. In this relation, the production term  $4\eta \delta^2$  is the strain heating, and the source term  $r$  denotes the volumetric heating due to radiation and tidal dissipation.

The above equations need to be complemented by dynamic and thermodynamic boundary conditions at the surface and the bottom of the respective ice body. If we assume that the surface is in contact with the atmosphere, then it can be described in good approximation as stress-free, that is,

$$\mathbf{t} \cdot \mathbf{n}|_s = \mathbf{0} \quad (33)$$

(where  $\mathbf{n}$  is the outer normal unit vector, and the subscript “s” denotes the surface). The surface temperature  $T_s$  can be prescribed directly as a Dirichlet condition.

If the bottom is a rigid ice/rock, ice/regolith or ice/sediment interface, no-slip conditions can be employed,

$$\mathbf{v}_b = \mathbf{0} \quad (34)$$

(the subscript “b” stands for the bottom). As for the temperature field, let us assume that the basal heat flux into the ice,  $\mathbf{q}_b$ , is known. This yields the Neumann condition

$$\kappa \frac{\partial T}{\partial \mathbf{n}} \Big|_b = \mathbf{q}_b, \quad (35)$$

where  $\mathbf{n}$  is again the outer normal unit vector.

The situation is different if the bottom is an ice/water interface. In this case, the basal stress conditions are governed by the hydrostatic pressure  $P_b$  of the water at the interface,

$$\mathbf{t} \cdot \mathbf{n}|_b = -P_b \mathbf{n}, \quad (36)$$

and the bottom temperature equals the pressure melting point,

$$T_b = T_m. \quad (37)$$

Provided that the role of impurities is negligible,  $T_m$  can be obtained from Eq. (1).

## 4 Polar caps of Mars

### 4.1 Large-scale simulations

The dynamic and thermodynamic state of the present-day polar caps of Mars will now be simulated with the ice-sheet model SICOPOLIS (“SIMulation COde for POLythermal Ice Sheets”). This model was developed in the mid-1990’s for terrestrial applications and has later been adapted to the north-polar cap of Mars (see [12], and references therein). It solves the ice-flow equations described in Sect. 3 based on the shallow-ice approximation [16, 22], that is, the flow regime is assumed to be simple, bed-parallel shear, the pressure is hydrostatic and lateral shear stresses as well as normal stress deviators are neglected (see also [3, this volume]). Inputs from the environment are specified by the mean annual surface temperature, the net surface mass balance (ice accumulation minus ablation) and the basal (“geothermal”) heat flux from the underlying lithosphere. The numerical solution of the model equations is carried out by a finite-difference integration technique.

Here, we only consider steady-state conditions, that is, the ice surface is held fixed as given by the Mars Orbiter Laser Altimeter (MOLA) data of the Mars Global Surveyor (MGS) spacecraft [32, 40]. This makes it unnecessary to prescribe the surface mass balance.

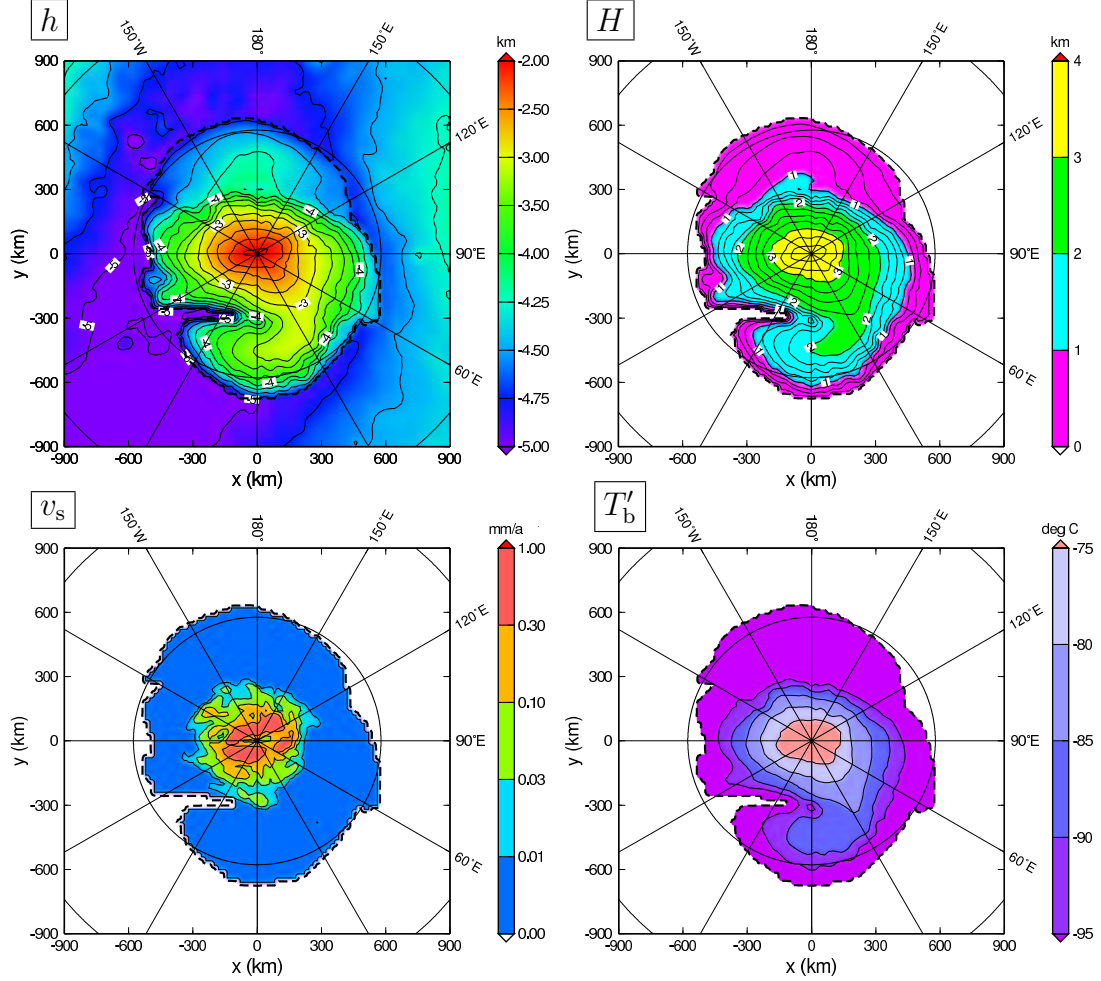


Figure 6: North-polar cap of Mars: MOLA surface topography  $h$  [32], computed ice thickness  $H$ , computed surface velocity  $v_s$  and computed homologous basal temperature  $T'_b$  for present-day steady-state conditions. Heavy-dashed lines indicate the ice-cap margin.

The topographies are shown in Figs. 6 and 7 (top left panels) for the north- and south-polar caps and their surroundings. It is striking that the overall shape of the north-polar cap is quite regular and smooth, whereas the south-polar cap appears much more rugged.

The ice temperature, velocity and bottom topography are allowed to evolve freely until the steady state is reached. Surface temperature is delivered by the model by Grieger (pers. comm. 2004; see also <http://www.space-vision.biz/marstemperatures.html>), which is based on a zonal and daily mean energy balance including a simple scheme for  $\text{CO}_2$  condensation and evaporation. Results agree well with those of the Martian Climate Database [21]; however, both methods fail in reproducing the observed year-round  $\text{CO}_2$  cover of the southern residual cap. Therefore, the southern mean-annual surface temperature is corrected such that it equals the  $\text{CO}_2$  sublimation temperature of  $-128^\circ\text{C}$  within  $85^\circ\text{S}$ . Further, the geothermal heat flux is assumed to be  $35 \text{ mW m}^{-2}$  [30], and the source term  $r$  in the temperature evolution equation (32) is neglected.

The unknown topography of the solid ground below the polar caps is computed in

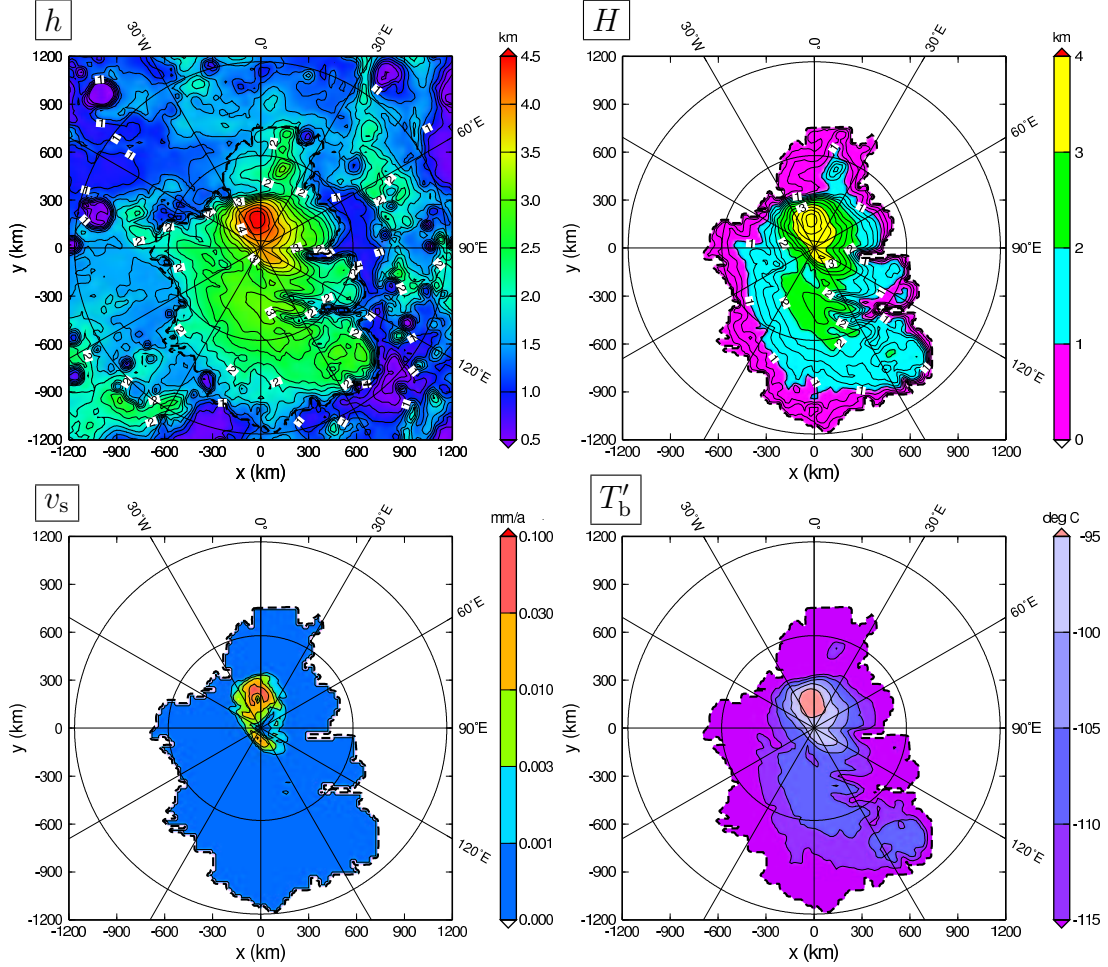


Figure 7: South-polar cap of Mars: MOLA surface topography  $h$  [32], computed ice thickness  $H$ , computed surface velocity  $v_s$  and computed homologous basal temperature  $T'_b$  for present-day steady-state conditions. Heavy-dashed lines indicate the ice-cap margin.

two steps. First, the equilibrated ground for ice-free conditions, which is required as a reference topography, is determined by a smooth extrapolation of the ice-free ground surrounding the north and south polar cap, respectively [13]. Second, the actual ground topography is obtained by superposing the isostatic deflection (downward displacement  $w$ ) of the underlying lithosphere due to the ice load. By modelling the lithosphere as a thin elastic plate, the isostatic deflection is governed by the bi-potential equation

$$K_1 \nabla^4 w = \rho g H - \rho_a g w, \quad (38)$$

where  $K_1 = 10^{25}$  N m is the flexural stiffness of the lithosphere,  $\nabla^4$  the bi-potential operator in the horizontal plane and  $\rho_a = 3500$  kg m $^{-3}$  the density of the asthenosphere (viscous mantle layer below the elastic lithosphere). The two load terms on the right-hand side are the ice load itself ( $\rho g H$ ) and the counteracting buoyancy force which the deflected lithosphere experiences from the asthenosphere below ( $\rho_a g w$ ). Note that the ice thickness  $H$  depends on  $w$  and is therefore part of the solution. In transient scenarios, which are

not considered here, the elastic deflection (38) is not assumed instantaneously, so that an additional evolution equation is required for the non-equilibrium displacement [11, 20].

The simulations have been carried out by applying Glen’s flow law as discussed in Sect. 2.3. The dust content is assumed to be 20% ( $\varphi_d = 0.2$ , see Sect. 2.5). Horizontal resolution is 20 km in the stereographic plane with standard parallel 71°N/S, vertical resolution is 51 grid points in the cold-ice column and 11 grid points in the lithosphere column, and the time-step is 1000 years.

Results for the ice thickness, the surface velocity and the homologous basal temperature are shown in Figs. 6 and 7 (top right and bottom panels) for both polar caps. The north-polar cap assumes its maximum thickness of 3.62 km almost exactly at the pole, whereas the maximum thickness of the south-polar cap, 3.88 km, is offset by approx. 150 km in 10°W direction. Of the entire ice volume of the NPC, which is  $1.53 \times 10^6 \text{ km}^3$ , a fraction of  $1.23 \times 10^6 \text{ km}^3$  (80%) is above the level of the equilibrated ground, and the remaining 20% are due to the isostatic deflection of the lithosphere. This ratio is almost the same for the SPC, with a total volume of  $2.30 \times 10^6 \text{ km}^3$  and a volume above the equilibrated ground of  $1.85 \times 10^6 \text{ km}^3$ .

Compared to terrestrial ice sheets and glaciers with typical flow velocities of tens to hundreds of meters per year, the flow of the Martian polar caps is very slow. The NPC reaches a maximum surface velocity of  $0.98 \text{ mm a}^{-1}$ , and south of 85°N surface velocities are everywhere less than  $0.01 \text{ mm a}^{-1}$ . Therefore, the active, dynamic zone only consists of the interior, thick part of the ice cap. The situation is even more extreme for the SPC, where the maximum surface velocity is as small as  $0.055 \text{ mm a}^{-1}$ , and by far the largest part of the ice cap flows at speeds slower than a micrometer per year (note the different scales of the colour bars). Therefore, the SPC can be considered as essentially stagnant.

Note that the 20-km resolution applied here does not resolve small-scale structures like the scarp/trough systems, which may lead to locally enhanced flow velocities. This will be discussed below (Sect. 4.2) for the NPC.

The slow flow velocities of the Martian polar caps lead to a conduction-dominated heat transport within the ice. The ratio of convection to conduction is given by the *Peclet number*

$$Pe = \frac{[U][L]}{[\alpha]}, \quad (39)$$

where  $[U]$  is a velocity scale,  $[L]$  is a scale of extent and  $[\alpha]$  is a scale for the thermal diffusivity  $\alpha = \kappa/(\rho c)$ . With  $[U] = 0.1 \text{ mm a}^{-1}$  for the NPC and  $0.01 \text{ mm a}^{-1}$  for the SPC, respectively,  $[L] = 300 \text{ km}$  (only the inner, dynamic region considered; see velocity panels of Figs. 6 and 7) and  $[\alpha] = 2 \times 10^{-6} \text{ m}^2 \text{ s}^{-1}$  (for  $-100^\circ\text{C}$  and 20% dust), one obtains Peclet numbers of  $Pe \approx 0.5$  for the NPC and  $Pe \approx 0.05$  for the SPC, respectively. Evidently, both values are less than unity, so that conduction outweighs convection. This leads to temperature profiles which increase essentially linearly with depth (not shown). By contrast, for terrestrial ice sheets and ice caps,  $Pe \gg 1$  always holds, so that their temperature fields are mainly governed by heat convection.

The different flow behaviour of the NPC and SPC is mainly due to the lower ice temperatures of the SPC, which are a consequence of the  $\sim 20^\circ\text{C}$  difference in surface temperatures. Since the thicknesses of both caps are similar, and the temperature distribution is mainly controlled by heat conduction, this transfers directly to a  $\sim 20^\circ\text{C}$  difference in average basal temperatures (again, note the different scales of the colour bars

in the respective panels of Figs. 6 and 7). The highest homologous basal temperatures are  $-69.1^{\circ}\text{C}$  for the NPC and  $-89.7^{\circ}\text{C}$  for the SPC, respectively, which demonstrates the insulating effect of the ice caps against the much colder surface temperatures. Nevertheless, the basal temperatures are in any case far below the pressure melting point. This is a very robust result, so that the presence of large amounts of subglacial liquid water as a potential habitat for Martian lifeforms can essentially be ruled out.

The simulation for the north-polar cap has been re-run with the alternative flow laws shown in Fig. 5 (GK with  $d = 1\text{ mm}$  and  $10\text{ mm}$ , Durham). As it was already found by Greve and Mahajan [12], this has a very significant influence on the computed flow velocities. The maximum surface velocity varies by almost three orders of magnitude, from the largest value  $3.02\text{ mm a}^{-1}$  for  $\text{GK}_{d=1\text{ mm}}$  via the above-mentioned  $0.98\text{ mm a}^{-1}$  for the reference simulation (Glen) and  $0.12\text{ mm a}^{-1}$  for  $\text{GK}_{d=10\text{ mm}}$  to only  $0.013\text{ mm a}^{-1}$  for Durham. As expected, this order corresponds to the low-stress regime in Fig. 5. Since the creep mechanism is probably a combination of dislocation creep (Glen, Durham) and grain-size-dependent creep (GK), we consider a value of the order of  $1\text{ mm a}^{-1}$  as most likely. By contrast, the basal temperature is virtually unaffected by the assumed flow law, which is a consequence of the dominance of flow-independent heat conduction over flow-dependent heat convection.

## 4.2 Detailed simulations of the scarps and troughs

In the large-scale simulations discussed above (Sect. 4.1), the spiralling scarps and troughs which cut up to several hundred meters into the surface of the Martian polar caps, have not been resolved. This was tackled in a study by Hvidberg [17], where a flowline of the north-polar cap extending from the pole in  $160^{\circ}\text{E}$  direction was investigated in detail, and an axisymmetric ice cap was assumed. The flowline was discretized by a finite-element grid at kilometer-scale horizontal resolution, and the ice-flow equations of Sect. 3 were solved without further approximations. Otherwise, the model set-up is very similar to that described in Sect. 4.1.

The temperature and flow fields computed by Hvidberg [17] are shown in Fig. 8. While the overall values agree very well with those reported above for the large-scale simulations (Sect. 4.1, Fig. 6), it becomes evident that the topographic disturbances imposed by the scarps/troughs result in significant disturbances of the ice flow which propagate all the way down to the bottom. The local flow accelerations are highlighted in Fig. 9, which shows the surface velocities and the surface mass balance required for maintaining the steady state. For the most pronounced trough about  $220\text{ km}$  away from the pole, the horizontal surface velocity is larger than  $15\text{ mm a}^{-1}$ , and even the vertical velocity reaches values of almost  $\pm 10\text{ mm a}^{-1}$ , distributed such that the trough would close in the absence of any mass exchange. In order to keep the troughs open, this must be balanced by a mass exchange at the surface such that ice accumulates outside the troughs, but is removed from within them at a rate of some millimeters per year (Fig. 9, bottom panel). This exchange pattern was already proposed by Fisher [8, 9] and termed “accublation model”. Physical processes behind the “accublation” exchange are likely differential ablation due to the albedo contrast (white material outside vs. darker material inside the troughs) and/or enhanced wind erosion due to the formation of local turbulences in the troughs.



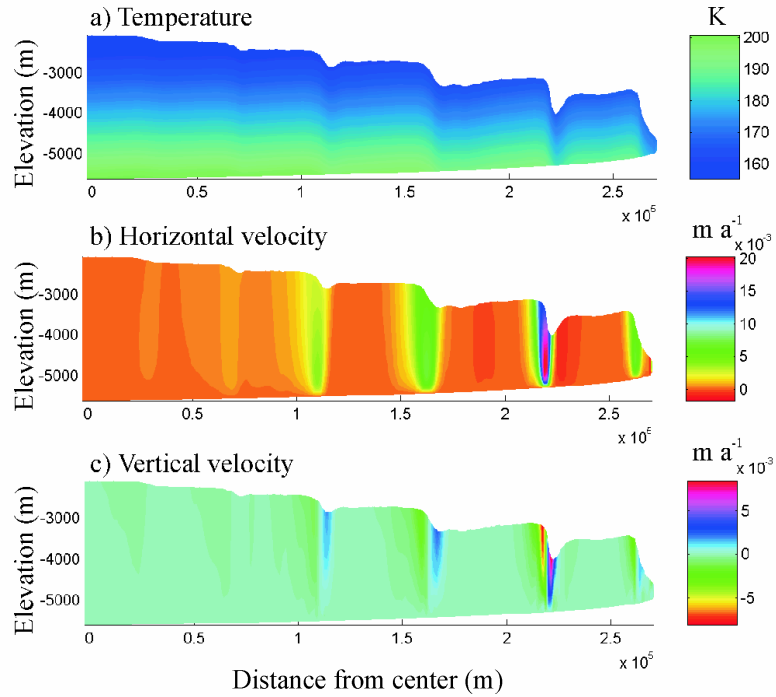


Figure 8: Computed temperature and velocity field of the north polar cap of Mars, for a flowline extending southward from the pole in  $160^\circ\text{E}$  direction. Figure by Hvidberg [17, her Fig. 2].

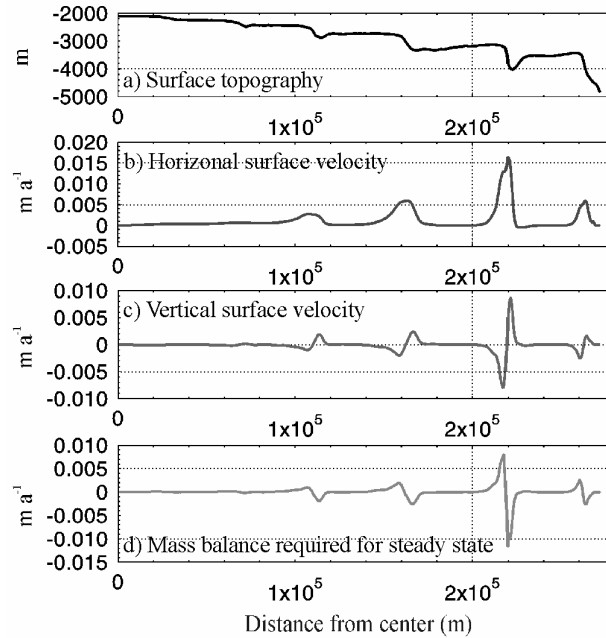


Figure 9: MOLA surface topography, computed surface velocity and computed steady-state mass balance corresponding to the simulation shown in Fig. 8. Figure by Hvidberg [17, her Fig. 3].

## 5 Icy shell of Europa

While the polar caps of Mars are localized ice masses on the planet’s surface which rest on solid land, the icy shell of Europa envelops the entire planetary body and is underlain most likely by a deep ocean. Also, the supposed thickness within the range of 10–50 km is much larger than that of the Martian polar caps. This allows the formation of convection cells, so that vertical motion may play a much larger role.

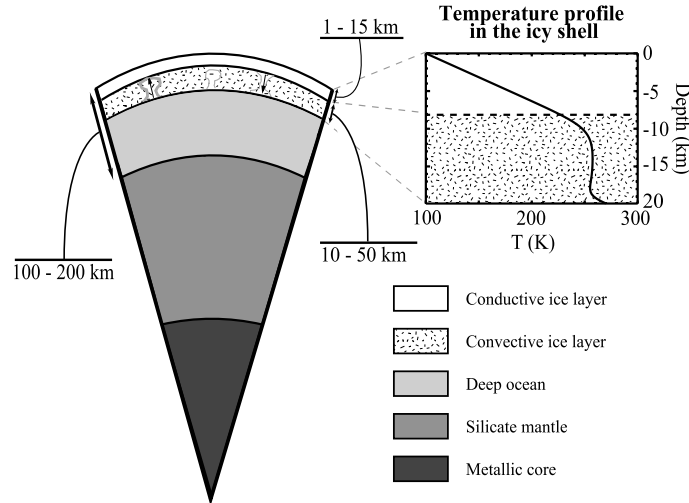


Figure 10: Model of the radial structure of Europa with a 20-km thick outer ice shell underlain by a deep ocean. The ice shell consists of an upper conductive lid and a lower convective layer. A possible temperature profile is shown in the inset plot. Figure by Tobie et al. [36, their Fig. 1].

Tobie et al. [36] investigated this problem by assuming a 20-km thick ice shell with a surface temperature of 100 K and a bottom temperature of 270 K, which is approximately equal to the pressure melting point (Fig. 10). The ice-flow equations of Sect. 3 are solved by finite differences in a two-dimensional cross-section of 40 km width, and the domain is treated as Cartesian. For the viscosity law, a simplified Newtonian viscosity is assumed, that is,  $n = 1$  and  $p = 0$  [see Eqs. (16) and (17)], and the dependence on the homologous temperature  $T'$  is modelled by an activation energy of  $Q = 50 \text{ kJ mol}^{-1}$ , which is close to the value of Goldsby and Kohlstedt [10]. The bottom viscosity is set to  $1.5 \times 10^{14} \text{ Pa s}$  in the reference simulation. The tidal dissipation  $r$  in the energy balance (32) is calculated by assuming a viscoelastic response of Europa to the tidal forcing, and the parameters of the Maxwellian rheology are prescribed variably in the four layers indicated in Fig. 10. This can lead to partial melting in the lower parts of the ice shell, the effect of which is accounted for by Eqs. (20)–(22). In the vertical component of the Stokes equation (29), the buoyancy force due the varying ice density, which results from partial melting and thermal expansion, is added.

The resulting fields of ice flow, temperature and tidal heating are shown in Fig. 11. As already sketched in Fig. 10, the huge temperature (and therefore viscosity) differences lead to the formation of an upper, conductive sublayer of approximately 8 km thickness,

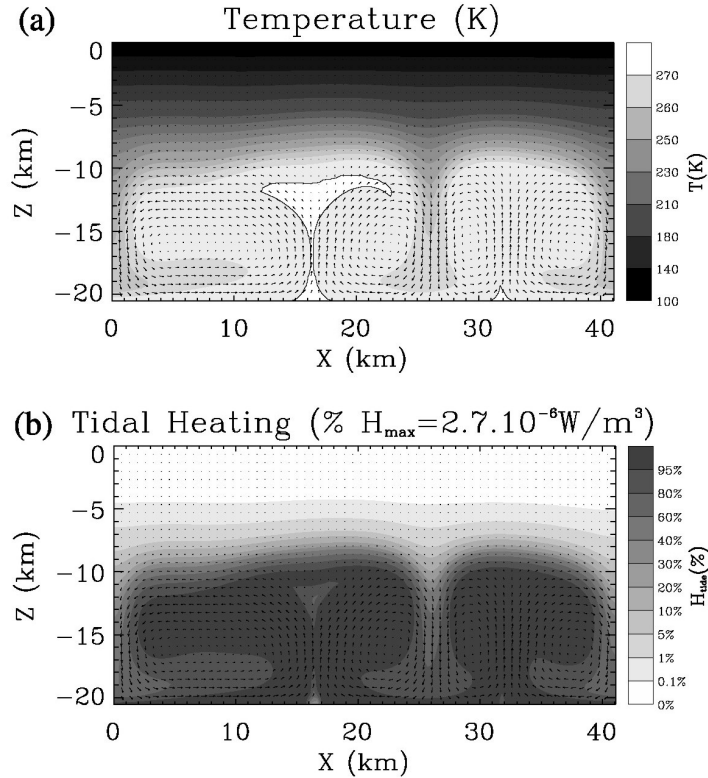


Figure 11: Computed flow field (arrows in both panels), temperature (panel a) and tidal heating (panel b) in Europa's ice shell for the reference simulation by Tobie et al. [36, their Fig. 4]. The solid contour in panel (a) delimits the area where the temperature is at the pressure melting point.

which is essentially rigid, and in which the temperature increases linearly with depth. By contrast, in the underlying convective sublayer significant ice flow occurs in the form of convection cells, with a maximum horizontal velocity of  $0.29 \text{ m a}^{-1}$ , a maximum upward velocity of  $0.265 \text{ m a}^{-1}$  and a maximum downward velocity of  $0.352 \text{ m a}^{-1}$ . Therefore, vertical temperature gradients are small in the convective sublayer. In the rising plumes, the ice temperature reaches the pressure melting point, and consequently partial melting occurs. The tidal heating is negligible in the upper, conductive sublayer, but reaches significant values up to  $2.7 \times 10^{-6} \text{ W m}^{-3}$  in the lower parts of the ice shell. It is also interesting to note that the convection cells entail large lateral gradients of the temperature and the tidal heating.

Fig. 12 shows the corresponding heat flux at the surface and the bottom of the ice shell (solid line in the plots). As it can be expected, the lateral variability of the heat flux at the surface is rather small, and the average value is approximately  $40 \text{ mW m}^{-2}$ . By contrast, at the bottom, the convection cells produce a heat-flux pattern highly variable in space and time (the latter is not shown in the snapshot figure) with an average of about one fourth of the surface heat flux.

In addition to the reference simulation discussed above, Tobie et al. [36] studied also the effects of different bottom viscosities, tidal dissipation rates (dashed line in Fig. 12,

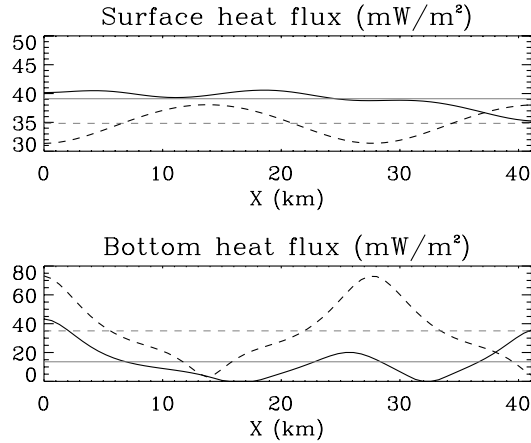


Figure 12: Surface and bottom heat flux corresponding to the simulation shown in Fig. 11 (solid line). The dashed line is for the same simulation without tidal heating [36, their Fig. 6].

etc.) and ice-shell thicknesses. This shall not be further reported here.

## 6 Concluding remarks

We have seen that water ice plays an important role in the climate systems of Earth and Mars. Further, it is a major constituent of the bulk volumes of the satellites of Jupiter, Saturn, Uranus and Neptune as well as the planet Pluto. The ice sheets, ice caps and glaciers on Earth and Mars show glacial flow, driven by their own weight. By contrast, ice flow driven by thermal convection can occur in the crust and interior of the icy satellites, depending on the temperature gradient between the warm interior and the cold surface. Here, we have limited the discussions to the “ordinary” ice Ih. However, at greater depths the occurrence of high-pressure phases can be expected, the rheology of which is poorly known.

Further “ices” made up of other moderately volatile substances are known or supposed to occur, for example, on Mars ( $\text{CO}_2$ ), Io ( $\text{SO}_2$ ), Europa, Ganymede and Callisto ( $\text{NH}_3$ ), Titan ( $\text{CH}_4$  and other carbohydrates), Triton and Pluto ( $\text{N}_2$ ,  $\text{CH}_4$ ). However, from a fluid-dynamical point of view, very little is known about their relevance, and it has not been possible to assess so far whether these materials are significant parts of flowing ice masses somewhere in the solar system.

## Acknowledgements

The author wishes to thank K. Hutter for his kind invitation to contribute this article to the current issue of the *GAMM-Mitteilungen*. Comments by R. Calov and K. Hutter on the draft version of the manuscript are gratefully acknowledged. Figure 1 reproduced by permission of Oxford University Press. Figure 2 reprinted with permission from Elsevier. Figures 8 and 9 reprinted from the *Annals of Glaciology* with permission of the

International Glaciological Society. Figures 10, 11 and 12 reproduced by permission of the American Geophysical Union.

## References

- [1] N. Azuma, Y. Wang, Y. Yoshida, H. Narita, T. Hondoh, H. Shoji and O. Watanabe. Crystallographic analysis of the Dome Fuji ice core. In: T. Hondoh, ed., *Physics of Ice Core Records*, pp. 45–61. Hokkaido University Press, Sapporo, Japan (2000).
- [2] W. V. Boynton, W. C. Feldman, S. W. Squyres, T. H. Prettyman, J. Bruckner, L. G. Evans, R. C. Reedy, R. Starr, J. R. Arnold, D. M. Drake, P. A. J. Englert, A. E. Metzger, I. Mitrofanov, J. I. Trombka, C. d’Uston, H. Wanke, O. Gasnault, D. K. Hamara, D. M. Janes, R. L. Marcialis, S. Maurice, I. Mikheeva, G. J. Taylor, R. Tokar and C. Shinohara. Distribution of hydrogen in the near surface of Mars: evidence for subsurface ice deposits. *Science* 297, 81–85 (2002).
- [3] R. Calov. Modelling of terrestrial ice sheets in paleo-climate research. *GAMM-Mitt.* 29, 9–28 (2006).
- [4] J. A. Church, J. M. Gregory, P. Huybrechts, M. Kuhn, K. Lambeck, M. T. Nhuan, D. Qin and P. L. Woodworth. Changes in sea level. In: J. T. Houghton, Y. Ding, D. J. Griggs, M. Noguer, P. J. van der Linden, X. Dai, K. Maskell and C. A. Johnson, eds., *Climate Change 2001: The Scientific Basis. Contribution of Working Group I to the Third Assessment Report of the Intergovernmental Panel on Climate Change*, pp. 639–693. Cambridge University Press, Cambridge etc. (2001).
- [5] S. M. Clifford, D. Crisp, D. A. Fisher, K. E. Herkenhoff, S. E. Smrekar, P. C. Thomas, D. D. Wynn-Williams, R. W. Zurek, J. R. Barnes, B. G. Bills, E. W. Blake, W. M. Calvin, J. M. Cameron, M. H. Carr, P. R. Christensen, B. C. Clark, G. D. Clow, J. A. Cutts, D. Dahl-Jensen, W. B. Durham, F. P. Fanale, J. D. Farmer, F. Forget, K. Gotto-Azuma, R. Grard, R. M. Haberle, W. Harrison, R. Harvey, A. D. Howard, A. P. Ingersoll, P. B. James, J. S. Kargel, H. H. Kieffer, J. Larson, K. Lepper, M. C. Malin, D. J. McCleese, B. Murray, J. F. Nye, D. A. Paige, S. R. Platt, J. J. Plaut, N. Reeh, J. W. Rice, D. E. Smith, C. R. Stoker, K. L. Tanaka, E. Mosley-Thompson, T. Thorsteinsson, S. E. Wood, A. Zent, Zuber M. T. and Zwally H. J. The state and future of Mars polar science and exploration. *Icarus* 144, 210–242 (2000).
- [6] W. B. Durham, S. H. Kirby and L. A. Stern. Creep of water ices at planetary conditions: A compilation. *J. Geophys. Res.* 102, 16293–16302 (1997).
- [7] W. C. Feldman, S. Maurice, D. J. Lawrence, R. C. Little, S. L. Lawson, O. Gasnault, R. C. Wiens, B. L. Barraclough, R. C. Elphic, T. H. Prettyman, J. T. Steinberg and A. B. Binder. Evidence for water ice near the lunar poles. *J. Geophys. Res.* 106, 23231–23251 (2001).
- [8] D. A. Fisher. If Martian ice caps flow – ablation mechanisms and appearance. *Icarus* 105, 501–511 (1993).

- [9] D. A. Fisher. Internal layers in an “accublation” ice cap: a test for flow. *Icarus* 144, 289–294 (2000).
- [10] D. L. Goldsby and D. L. Kohlstedt. Grain boundary sliding in fine-grained ice I. *Scripta Materialia* 37, 1399–1406 (1997).
- [11] R. Greve. Glacial isostasy: Models for the response of the Earth to varying ice loads. In: B. Straughan, R. Greve, H. Ehrentraut and Y. Wang, eds., *Continuum Mechanics and Applications in Geophysics and the Environment*, pp. 307–325. Springer, Berlin etc. (2001).
- [12] R. Greve and R. A. Mahajan. Influence of ice rheology and dust content on the dynamics of the north-polar cap of Mars. *Icarus* 174, 475–485 (2005).
- [13] R. Greve, R. A. Mahajan, J. Segsneider and B. Grieger. Evolution of the north-polar cap of Mars: a modelling study. *Planet. Space Sci.* 52, 775–787 (2004).
- [14] C. U. Hammer, H. B. Clausen, W. Dansgaard, A. Neftel, P. Kristinsdottir and E. Johnson. Continuous impurity analysis along the Dye 3 deep core. In: C. C. Langway, H. Oeschger and W. Dansgaard, eds., *Greenland Ice Core: Geophysics, Geochemistry and the Environment*, Geophysical Monographs No. 33, pp. 90–94. American Geophysical Union, Washington DC (1985).
- [15] J. W. Head, J. F. Mustard, M. A. Kreslavsky, R. E. Milliken and D. R. Marchant. Recent ice ages on Mars. *Nature* 426, 797–802 (2003).
- [16] K. Hutter. *Theoretical Glaciology; Material Science of Ice and the Mechanics of Glaciers and Ice Sheets*. D. Reidel Publishing Company, Dordrecht, The Netherlands (1983).
- [17] C. S. Hvidberg. Relationship between topography and flow in the north polar cap on Mars. *Ann. Glaciol.* 37, 363–369 (2003).
- [18] J. S. Kargel, J. Z. Kaye, J. W. Head, G. M. Marion, R. Sassen, J. K. Crowley, O. P. Ballesteros, S. A. Grant and D. L. Hogenboom. Europa’s crust and ocean: Origin, composition, and the prospects for life. *Icarus* 148, 226–265 (2000).
- [19] J. Laskar, A. C. M. Correia, M. Gastineau, F. Joutel, B. Levrard and P. Robutel. Long term evolution and chaotic diffusion of the insolation quantities of Mars. *Icarus* 170, 343–364 (2004).
- [20] E. Le Meur and P. Huybrechts. A comparison of different ways of dealing with isostasy: examples from modelling the Antarctic ice sheet during the last glacial cycle. *Ann. Glaciol.* 23, 309–317 (1996).
- [21] S. R. Lewis, M. Collins, P. L. Read, F. Forget, F. Hourdin, R. Fournier, C. Hourdin, O. Talagrand and J.-P. Huot. A climate database for Mars. *J. Geophys. Res.* 104, 24177–24194 (1999).

- [22] L. W. Morland. Thermomechanical balances of ice sheet flows. *Geophys. Astrophys. Fluid Dyn.* 29, 237–266 (1984).
- [23] J. F. Nye. The distribution of stress and velocity in glaciers and ice sheets. *Proc. R. Soc. Lond. A* 239, 113–133 (1957).
- [24] J. F. Nye. A flow model for the polar caps of Mars. *J. Glaciol.* 46, 438–444 (2000).
- [25] W. S. B. Paterson. *The Physics of Glaciers*. Pergamon Press, Oxford etc., 3rd edition (1994).
- [26] V. F. Petrenko and R. W. Whitworth. *Physics of Ice*. Oxford University Press, Oxford etc. (1999).
- [27] E. C. Pettit and E. D. Waddington. Ice flow at low deviatoric stress. *J. Glaciol.* 49, 359–369 (2003).
- [28] L. Placidi, K. Hutter and S. H. Faria. A critical review of the mechanics of polycrystalline polar ice. *GAMM-Mitt.* 29, 80–117 (2006).
- [29] M. E. Raymo, D. W. Oppo and W. Curry. The mid-Pleistocene climate transition: A deep sea carbon isotopic perspective. *Paleoceanogr.* 12, 546–559 (1997).
- [30] G. Schubert, S. C. Solomon, D. L. Turcotte, M. J. Drake and N. H. Sleep. Origin and thermal evolution of Mars. In: H. H. Kieffer, B. M. Jakosky, C. W. Snyder and M. S. Matthews, eds., *Mars*, pp. 147–183. University of Arizona Press, Tucson (1992).
- [31] M. A. Slade, B. J. Butler and D. O. Muhleman. Mercury radar imaging – evidence for polar ice. *Science* 258, 635–640 (1992).
- [32] D. E. Smith, M. T. Zuber, S. C. Solomon, R. J. Phillips, J. W. Head, J. B. Garvin, W. B. Banerdt, D. O. Muhleman, G. H. Pettengill, G. A. Neumann, F. G. Lemoine, J. B. Abshire, O. Aharonson, C. D. Brown, S. A. Hauck, A. B. Ivanov, P. J. McGovern, H. J. Zwally and T. C. Duxbury. The global topography of Mars and implications for surface evolution. *Science* 284, 1495–1503 (1999).
- [33] F. Sohl, H. Hussmann, B. Schwentker, T. Spohn and R. D. Lorenz. Interior structure models and tidal Love numbers of Titan. *J. Geophys. Res.* 108, 5130 (2003).
- [34] P. Thomas, S. Squyres, K. Herkenhoff, A. Howard and B. Murray. Polar deposits of Mars. In: H. H. Kieffer, B. M. Jakosky, C. W. Snyder and M. S. Matthews, eds., *Mars*, pp. 767–795. University of Arizona Press, Tucson (1992).
- [35] T. Thorsteinsson. Textures and fabrics in the GRIP ice core, in relation to climate history and ice deformation. *Reports on Polar Research* No. 205. Alfred Wegener Institute for Polar and Marine Research, Bremerhaven (1996).
- [36] G. Tobie, G. Choblet and C. Sotin. Tidally heated convection: Constraints on Europa’s ice shell thickness. *J. Geophys. Res.* 108, 5124 (2003).

- [37] C. J. van der Veen. Fundamentals of Glacier Dynamics. A. A. Balkema, Rotterdam (1999).
- [38] W. Wagner, A. Saul and A. Pruß. International equations for the pressure along the melting and along the sublimation curve of ordinary water substance. J. Phys. Chem. Ref. Data 23, 515–527 (1994).
- [39] K. Watson, B. C. Murray and H. Brown. The stability of volatiles in the solar system. Icarus 1, 317–327 (1963).
- [40] M. T. Zuber, D. E. Smith, S. C. Solomon, J. B. Abshire, R. S. Afzal, O. Aharonson, K. Fishbaugh, P. G. Ford, H. V. Frey, J. B. Garvin, J. W. Head, A. B. Ivanov, C. L. Johnson, D. O. Muhleman, G. A. Neumann, G. H. Pettengill, R. J. Phillips, X. Sun, H. J. Zwally, W. B. Banerdt and T. C. Duxbury. Observations of the north polar region of Mars from the Mars Orbiter Laser Altimeter. Science 282, 2053–2060 (1998).

## A Pressure dependence of ice flow

The flow rate factor (8) can be written as

$$\begin{aligned}
 A(T') &= A_0 \exp\left(-\frac{Q}{RT'}\right) \\
 &= A_0 \exp\left(-\frac{Q}{R(T + \beta P)}\right) = A_0 \exp\left(-\frac{Q}{RT(1 + \beta P/T)}\right), \quad (40)
 \end{aligned}$$

where the linearized melting-point depression (3) has been used for simplicity. For the stability range of ice Ih,  $P \lesssim 200$  MPa, we have  $\beta P < 20$  K, and therefore  $\beta P/T \ll 1$ . This allows the Taylor approximation

$$A(T') = A_0 \exp\left(-\frac{Q}{RT}\left(1 - \frac{\beta P}{T}\right)\right) = A_0 \exp\left(-\frac{1}{RT}\left(Q - \frac{Q\beta P}{T}\right)\right). \quad (41)$$

By comparing this with the flow rate factor in the general form (5), the activation volume which corresponds to the simplified form (8) is

$$PV = -\frac{Q\beta P}{T} \quad \Rightarrow \quad V = -\frac{Q\beta}{T}. \quad (42)$$

For  $Q = 60$  kJ mol<sup>-1</sup> and  $T = 200$  K, this yields  $V = -2.94 \times 10^{-5}$  m<sup>3</sup> mol<sup>-1</sup>, which agrees well with the (quite uncertain) values reported by Paterson [25],  $V = -1.7 \times 10^{-5}$  m<sup>3</sup> mol<sup>-1</sup>, and by Durham et al. [6],  $V = -1.3 \times 10^{-5}$  m<sup>3</sup> mol<sup>-1</sup>. Therefore, the pressure dependence of the flow rate factor is described reasonably well by the simplified form (8) which depends on the homologous temperature only.